Real-time two dimensional dosimetry using Al_2O_3:C and Al_2O_3:C,Mg films

Reference:
de Nascimento Luana F., Goossens Jo, Leblans Paul, Sterckx Paul, Vanhavere Filip, Struelens Lara, Akselrod Mark, Verellen Dirk.- Real-time two dimensional dosimetry using Al_2O_3:C and Al_2O_3:C,Mg films
Sensors and actuators : A : physical - ISSN 0924-4247 - 318(2021), 112491
Full text (Publisher's DOI): https://doi.org/10.1016/J.SNA.2020.112491
To cite this reference: https://hdl.handle.net/10067/1766280151162165141

Real-time dosimetry using Al_2O_3:C and Al_2O_3:C,Mg films

Luana de F. Nascimento[1]*, Jo Goossens[2], Paul Leblans[3], Paul Sterckx[3], Filip Vanhavere[1], Lara Struelens[1], Mark Akselrod[4], Dirk Verellen[2]

[1]Belgian Nuclear Research Centre, Mol, Belgium
[2]Iridium Kankernetwerk; University of Antwerp, Antwerp, Belgium
[3]Agfa NV, Mortsel, Belgium
[4]Landauer, Stillwater Crystal Growth Division, Stillwater, USA
**ldfnasci@sckcen.be*

Abstract

The Investigations of this article focus on the response of Al_2O_3:C and Al_2O_3:C,Mg radioluminescence films for medical dosimetry in various MV photon beams. A dosimetry system was configured using a scientific camera, attached to the head of the linear accelerator (LINAC), facing the beam's isocenter, where the films were placed. By using the appropriate filter and lens it is possible to measure real time two-dimensional dose-rate distributions. The key findings are that Al_2O_3:C,Mg films present a clear advantage compared to Al_2O_3:C ones, with no interference from afterglow, better film uniformity, high spatial resolution and suitability for small field beam dosimetry, while giving overall good dose-rate response in Flattening Filter (FF) and Flattening Filter Free (FFF) modes. The results show that our system can be used for planar real time dose rate assessment in medical photon dosimetry with manageable correction factors.

1. Introduction

Radioluminescence (RL) and scintillation processes involve energy conversion, thermalization, transfer to luminescent centres and finally light emission. The light emission that occurs at a particular wavelength, reaches a peak of emission and decays to 1/e value of its peak intensity in 5 microseconds or less is arbitrarily termed a scintillation light and the solid a "Scintillator", the rest are designated as "Phosphors" that emits "radioluminescence" signal with long decay of light after the exciting source has been removed. ~~Radioluminescence (RL) is the phenomenon of light emission by dielectric and semiconductor materials upon excitation of lattice defects, either initially present within the material as impurities or vacancies, or induced by radiation through displacement damage~~ [1]. Detection ~~of this luminescence~~ of prompt luminescence during megavoltage external beam radiotherapy could be applied for superficial dose estimation, functional imaging, and patient specific quality assurance (QA) for radiation therapy dosimetry.

Recent studies have exploited the use of RL materials and scintillators for measuring real-time in situ dose information in radiotherapy. Several of these dosimeters are based on ~~small RL or plastic scintillator~~ detectors ~~(PSDs)~~ coupled to plastic or silica optical fibres [2]. These optical fibres are mostly used as a light guide of the luminescence generated during irradiation to a detector and the probes are made light tight to avoid interference from external light [3-7]. These point detectors present several advantages, such as high spatial resolution, stability, flexibility, low cost, real time measurement and potential for small field dosimetry applications [2]. In addition to the ever-growing scientific literature on this subject, RL and scintillator devices are also becoming commercially available [8, 9].

Both RL and scintillator ~~PSD~~ systems have many desirable properties for dosimetry applications; however, they are susceptible to stem effects, caused especially by the emission of Cerenkov light from the optical guide fibre. Several attempts were made to solve this problem by using, for example, a two-fibre subtraction method (one fibre with and one without ~~RL/PSD~~ detector) [10], a spectral filtering and chromatic removal techniques [11]. In addition, others described the possibility to use Cerenkov light for beam dose measurements [12].

Attempts to design real time one-dimensional (1D) or two-dimensional (2D) systems using RL/scintillator ~~PSD~~+fibre detectors are based on multiple single-probe arrays, packed closely together [13-18]. A more recent alternative for 2D dosimetry using films containing ~~RL/PSD~~ luminescent materials [2, 19] has been reported. As an alternative to using optical fibres, the luminescence is directly measured by using photomultipliers, photodiodes or cameras. This approach attempts to visualize the position, shape, and intensity of the radiation beam as it passes through the 2D film. This solution has potential for *in vivo* dosimetry, for transmission dosimetry, for creating transit 2D images and for patient and machine quality assurance (QA).

Pre-treatment QA is the least sensitive tool out of all control checks to detect errors in radiation oncology [20], as it misses, for instance, errors in patient positioning, necessary adaptations between fractions and machine malfunctioning. These aspects highlight the need for patient-specific QA and requires *in vivo* dosimetry tools. A real time system, based on coated Al_2O_3:C or Al_2O_3:C,Mg films, have the potential for fast, reliable and easy dose assessment. Coated films can be made very thin and flexible, to cover patients skin or to be coated in immobilization devices.

In this work, we present the dosimetric characterization and proof of concept of a real-time 2D RL system in external beam radiotherapy, by comparing distinct films coated with Al_2O_3:C or Al_2O_3:C,Mg [21, 22]. Al_2O_3:C is a well stablished optically stimulated luminescence (OSL) material [23], while Al_2O_3:C,Mg has gained attention as radiophotoluminescence (RPL) and optical imaging material [24]. The imaging system presented in this work consists of a camera positioned to face the isocenter of the linear accelerator beam to detect luminescence being emitted by the 2D RL films. The intensity of RL emission is directly proportional to the radiation dose rate.

2. Materials and Methods

The 2D dosimetric system consisted of a flexible RL film containing either Al_2O_3:C or Al_2O_3:C,Mg micro crystals and a digital camera. The film can be placed in several locations, such as in free air, on a phantom surface or under transparent Poly(methyl methacrylate) (PMMA) plates. The films emit light (RL) when exposed to ionizing radiation. The camera is placed at the head of the LINAC, facing the isocenter.
Al_2O_3:C and Al_2O_3:C,Mg material for dosimetric applications was produced by Landauer Inc. in the form of single crystals and powders of different grain sizes. Al_2O_3 was grown in a highly reducing atmosphere in the presence of carbon under carefully controlled conditions, in such a way that Al_2O_3:C was formed with high concentrations of F and F+ centres (≈$3x10^{17}$ cm^{-3} and ≈$7x10^{15}$ cm^{-3}, respectively) [25]. To grow Al_2O_3:C,Mg, Mg dopants were also used during crystal growth to modify the concentration and energy distribution of traps in the material. The concentration of Mg-impurities in the crystals was in the range of 8–27 ppm [24] and resulted in aggregate defects consisting of two oxygen vacancies and two Mg-impurities, in addition to F and F+ centres in different concentration, compared to Al_2O_3:C [21].
The two materials present different color centers and emit luminescence at different wavelengths. Al_2O_3:C F-centers have 35 ms lifetime, while the Mg-doped crystal (Al_2O_3:C,Mg) have much faster color centers in addition to F centers and produce luminescence with 9 and 75 ns decays time [22, 24].

2.1. Films

Four types of films were tested, as described in Table 1. The main difference between the films was the nature and the crystal size of the RL material (Al_2O_3:C or Al_2O_3:C,Mg), and the coating process. The two types of crystals used were grown by Landauer Inc., and the films were manufactured by AGFA NV (Belgium) or Landauer Inc (USA). The films were Al_2O_3:C,Mg powder grains coated in the polymer binder deposited on a water equivalent substrate of white or transparent (Trans-) Polyethylene terephthalate (PET). Coatings without Al_2O_3:C or Al_2O_3:C,Mg irradiated with the highest dose-rate from the LINAC did not result in measurable RL signal.

Table 1. Overview of films based on Al_2O_3:C and Al_2O_3:C,Mg, indicating the RL material crystal size, film thickness, coating type, dimensions, producer and samples' abbreviated name.

Material	Average crystal size (µm)	Film thickness (µm)	Substrate	Substrate vs Crystal ratio	Dimensions (cm^2)	Producer	Abbreviated name
Al_2O_3:C	25	75	Trans-PET	4/96	21 x 29	Landauer	L-C
Al_2O_3:C	2.5	115	White-PET	4/96	10 x 10	AGFA	A-C
Al_2O_3:C,Mg	25	75	Trans-PET	4/96	21 x 29	Landauer	L-CMg
Al_2O_3:C,Mg	7	75	White-PET	4/96	10 x 10	AGFA	A-CMg

2.2. Irradiations

The external beam irradiator for this study was a TrueBeam STx (Varian Medical Systems, Palo Alto, CA) We used photons of 6, 10 and 15 MV in beams with Flattening Filter (FF) and of 6 and 10 MV in Flattening Filter Free mode (FFF). Squared field sizes ranged from 10 x 10 mm^2 to 100 x 100 mm^2. The LINAC was calibrated using the NCS report 18 [26] to obtain an equivalence of 1 cGy/1 monitor unit (MU) at depth of maximum dose (d_{max}) in reference conditions, for a 100 x 100 mm^2 field size and a 100 cm source-to-surface distance (SSD). The various measurements were performed in combination with a series of PMMA transparent slab phantoms.

2.3. Image processing and tests

The Kite (Raptor) electron multiplying charge-coupled device (EMCCD) camera was controlled by the µManager software [27] and image processing was done using ImageJ and Fiji [28]. To correct the acquired images from the off-normal angle (≈ 10º) to normal angle, we used the Interactive Perspective plugin from Fiji [29]. For all the tests, square fields were used for general system characterization. Short pass filters are used to block ambient light and let only the short range of the radioluminescence emission reach the camera sensor, improving the optical discrimination and signal to noise ratio of our system.
The pixels from the images were transformed to a calibrated image space using markers in the phantom and LINAC

light field edges, so that each pixel corresponded to 0.1 x 0.1 mm^2. When necessary, parts of the image were smoothed by a noise filter to remove values of saturated pixels caused by high-energy scattered photons. The ΔRL signal used for the dosimetric characterizations of each film was generated from averaged RL images acquired during irradiation (in a specific region of interest - ROI) subtracted by the averaged background (B) signal. Background images were acquired by averaging images prior and post irradiation at the same sampling rate used for the images acquired during irradiation (around 40 images). The standard deviation (SD) of background light (prior and post-irradiation) did not exceed 1% in all the tests presented in this study. We used as default the camera sampling rate of 20 ms.
Most of the tests were performed using 6 MV FF photon beam, 100 x 100 mm^2 field size (defined by the jaws), 600 MU/min, 100 MU, under a 1.5 cm transparent PMMA slab (300 mm x 300 mm x 15 mm) to reach d_{max} at SSD = 100 cm. Different dose, dose-rate, field sizes and beam energies are mentioned in each test, when necessary.
The **films' quality** was assessed by exposing the four types of films (Table 1) to 400 MU/min. Contrast-to-noise ratios (CNRs) [30] were calculated by dividing the average pixel intensity (ΔRL) of a ROI of 10 x 10 mm^2 centred in the bright region of the irradiated image by the standard deviation of the background image (sd_B), with the same ROI (equation 1).

$$CNR = \frac{Contrast}{Noise} = \frac{[\overline{RL} - \overline{B}]}{sd_B} = \frac{\Delta RL}{sd_B} \text{ (equation 1)}$$

The **films' uniformity** was assessed in a specific ROI (10 x 10 mm^2) by calculating the coefficient of variation (COV) as a function of different dose-rates. The film uniformity was evaluated for films exposed to 10, 50, 100, 300 and 600 MU/min.
To determine the films' **spatial resolution** line pattern images were acquired using a polytetrafluoroethylene solid plate (Teflon), with four narrow slits, two with 1 mm width (1 mm apart) and two with 1.5 mm (3 mm apart), placed on top of the A-CMg film. The resolution was characterized calculating the point spread function (PSF), from the average from ten profiles crossing the centre of the image (0.5 mm x 10). The results are presented in terms of Full-Width-at-Half-Maximum (FWHM) values, which are the most common way to specify PSF [31].
Afterglow is measured with normalized RL counts (to the maximum signal) from the two films coated by AGFA (A-CMg and A-C), in response to an irradiation with 1 minute of duration. The beam is turned off at time $t = t_{1\ min} + 0.37$ seconds and the signal from the films was recorded within a time interval of 20 ms, up to 100 ms.
Dose rate measurements were made by comparing the measured light intensity (ΔRL) at different given dose rates using 6, 10 and 15 MV photon beams in FF and 6 and 10 MV in FFF mode. The degree of the films' dose-rate linearity was evaluated by measuring the average ΔRL from a 10 x 10 mm^2 ROI and normalizing the results to 400 MU/min data. Reference data was acquired using a Semiflex ionization chamber (PTW). A statistical evaluation of the dose-rate dependence on the films response for all energies was performed through the Student's t-test of the linear regression [32]. The smaller the Prob>|t| (p-value), the more unlikely the parameter is equal to zero. The null hypothesis of t-test is rejected if [Prob>|t|] < 5%. An additional test looked into the relation between RL signals and LINAC **individual dose per pulse**, for the minimum dose-rates (FF mode) described in Table 2.
Small squared fields and output factors were measured for a range of field sizes, defined using the multi leaf collimator. More specifically, five fields were measured with sizes of 10 x 10, 30 x 30, 50 x 50, 70 x 70 and 100 x 100 mm^2. The output factors were normalized to the corresponding central axis for the 100 x 100 mm^2 field size.

Table 2. TrueBeam and nominal photon energies, maximum dose rate and dose per beam pulse.

Nominal photon beam energy (MV)	Maximum dose rate (Gy/min)	Minimum dose rate (Gy/min)	Dose per beam pulse (mGy/pulse)
6 FF	6	0.05	0.28
10 FF	6	0.05	0.28
15 FF	6	0.20	0.56

3. Results and discussion

3.1. RL intensity and image quality

Images of the four types of films are presented in Figure 1. Images show clear differences in intensities, while all showing uniformity across the field and clear boundaries. When comparing the Al_2O_3:C,Mg films, L-CMg and A-CMg differ in light intensity, with the film from AGFA presenting a RL signal twice as high as the film from Landauer. The thickness of the coated layer in both films is the same (75 μm), but the grain size is different and density (load) of crystaline grains per unite area of L-CMg is smaller than in A-CMg film (see Table 1).The crystal size differs with 25 µm (L-CMg) and 7 µm (A-CMg) and the micro crystals come from the same manufacturer, but the concentration of active material, and the homogeneities of the coatings are different.

The same is observed for the Al_2O_3:C films, with differences in RL intensities. The crystal sizes are different (25 µm and 2.5 µm) as well as the film thicknesses (75 µm vs 112 µm). The A-C sheet has around 50% higher RL intensity than the L-C. The average, standard and CNR deviation from a 10 x 10 mm^2 ROI centred in the main field is presented in Table 3.

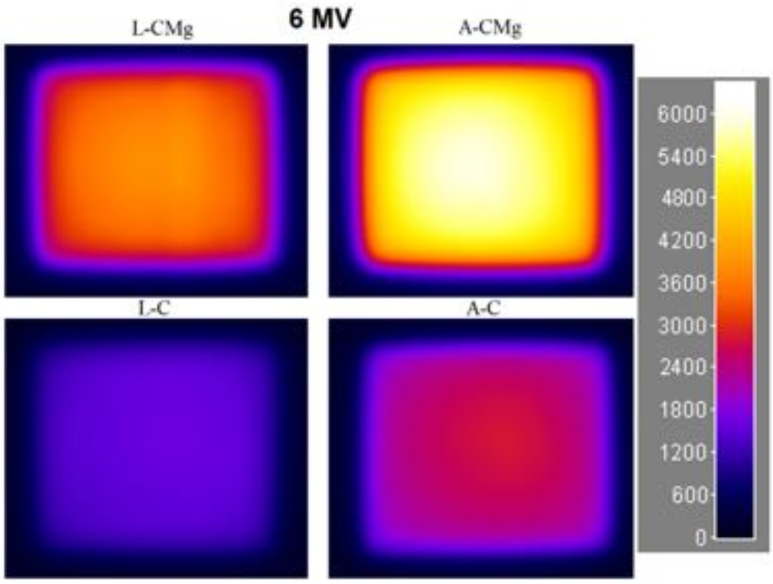

Figure 1. Images of four film types irradiated with 70 x 70 mm^2 fields, 600 MU/min, 6 MV. RL and background intensities are reported in pixel values (arbitrary units).

Table 3. Overview of films' quality, with background average and standard deviation, RL average and standard deviation and contrast-to-noise ratio.

Sheet	*Background Average [counts]*	*Background SD [counts]*	*RL average [counts]*	*RL SD [counts]*	*Contrast-to-noise ratio (CNR)*
L-C	118	32	1213	100	34
A-C	115	27	3173	75	113
L-CMg	116	29	4266	115	143
A-CMg	119	31	5411	80	170

Figure 2 shows how the CNR can be easily visualized and interpreted using image histograms. The histograms of all four images (from Figure 1) are set such that the contrast and brightness are adjusted so that the peak distribution of dark pixels in the images are at the same location. Under this condition, the peak at the right side from A-CMg ("bright pixels") shifts to the far right compared to L-C, with L-CMg and A-C in between. This means that image A-CMg has the highest contrast (wider distance between the peaks) under the condition of equal noise (dark peak), i.e. higher CNR; followed by L-CMg, A-C and L-C. The CNR is independent of contrast and brightness values, as long as the pixels are not saturated [33].

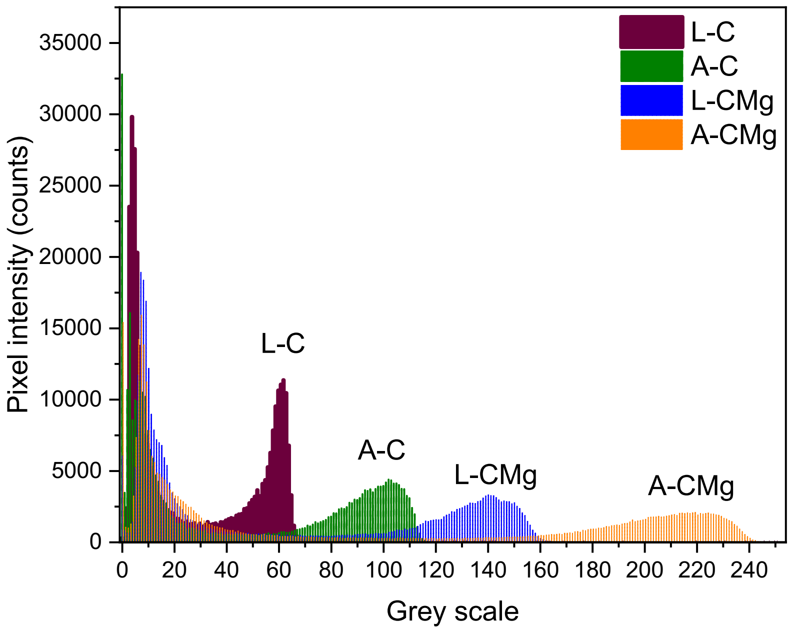

Figure 2. Contrast-to-noise-ratio histograms from the fours film types (L-C, A-C, L-CMg and A-CMg). The distribution peaks of dark pixels of the images are at the same location and no image presented pixel saturation.

Our results show that A-CMg has almost four times better CNR than L-C. The CNR has been extensively used in medical imaging [34, 35] and quality assurance [36, 37] and presents a better image quality measure than the signal-to-noise ratio (SNR) analysis. For example, a gaseous scintillation detector readout using a charge-coupled device camera [38] shows image quality intensity variations of up to 10%, caused by Gas Electron Multiplier-hole variations and its non-flat surface; while, in another work a YAG:Ce scintillation single crystal with a low noise camera is compared to a Medipix detector, showing that the Medipix can achieve two to three times better CNR [39].

3.2. Film uniformity

The films' uniformities (% COV) as a function of dose-rate are shown in Figure 3. The Landauer films (L-C, L-CMg) present, overall, a lower homogeneity than the AGFA films (A-C, A-CMg). The Agfa films were produced from later and more homogeneously doped Landauer crystals. For example, the pixel intensities obtained at 10 MU/min for the Landauer films cannot be distinguishable from the background images. On average, all films present constant COV for dose-rates ≥ 100 MU/min. The coefficient of variation improves with dose-rate due to an increase in the RL signal and, therefore, leads to a better CNR. A local non-uniformity of 5 and 7% is observed for 10 MU/min dose-rate for A-CMg and L-CMg, respectively, while it is on average 1% and 3% for dose-rates above 50 MU/min. The higher COV at low dose rates is the result of lower pixel count statistics per image frame and can be improved by increasing the camera exposure time. For the subsequent tests, we focus on the AGFA films and compare Al_2O_3:C to Al_2O_3:C,Mg, as these films present better CNR and uniformity.

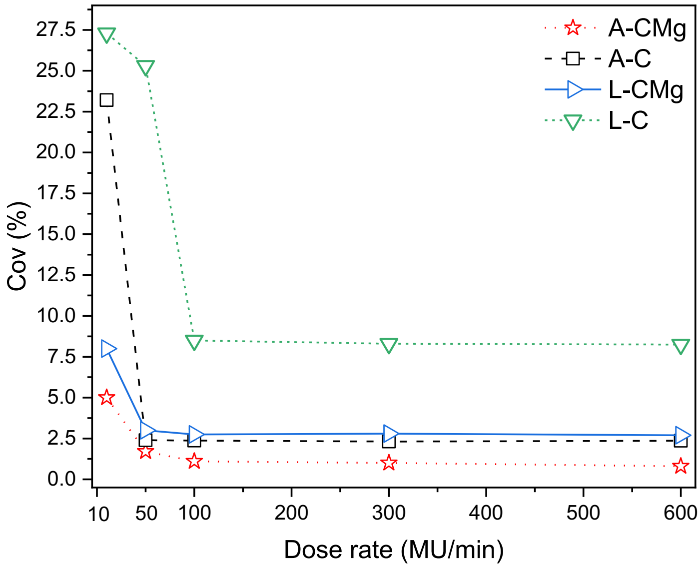

Figure 3. COV (%) vs. dose rate (MU/min) from the four type of films (table 1).

Uniformity is a key characteristic for good 2D dosimetry. The thickness and the concentration of crystals in the radiosensitive coating from our films can affect the correlation at a local level, as observed in Figure 3. The standard films used in QA, the GAFChromic EBT3 and EBT2 films, can reach uniformity uncertainties below 1.0% [40, 41], for time periods between irradiating and scanning of 21 h to 27 h. For real time measurements, uniformity is a combination of film quality and read out method. Jenkins et al. [19] presented a system similar to ours, with sufficient resolution to distinguish individual multileaf collimator (MLC) leaves as good as 1 mm for irradiations with 6 MV. No information is, however, given for dose rates lower than 200 MU/min.

3.3. Spatial resolution

Figure 4a presents the image resulting from irradiating the Teflon plate, on top of the A-CMg film, with 600 MU/min 6MV. One can observe four bright lines, from top to bottom, resulting from the RL emission passing through the slits. Figure 4b shows the plot from the profile crossing the slits (line L in Figure 4a), presenting normalized RL signal vs. length. The dark region of the Teflon is, in average, 3% compared to the brightest RL peak (slit 1). Slits peaks 2, 3 and 4 are, respectively, 99.5, 97.5 and 99.5%, when compared to slit 1 (100%).
The average FWHM and difference between calculated and actual width from ten profiles, adjacent to and included in the plotted line L, are listed in Table 4. The FWHM from all the slits are slightly higher than the nominal thickness, with precision of 0.1 mm.
A previous work presenting a 2D RPL acquisition system based on Al_2O_3:C,Mg film had a spatial resolution of 0.92 mm [42], nonetheless, the films used were similar to the L-CMg, which means larger crystals grain sizes, worse uniformity and lower image quality when compared to A-CMg. Additionally, the EMCCD camera has a higher intrinsic spatial resolution compared to the spot size of the laser diode used to excite the RPL films [43].
Gafchromic films, the most common commercial 2D planar system used in radiotherapy, has a sub-mm spatial resolution [40, 44]. However, such systems are not real time, require cumbersome calibration and/or need several corrections to compensate for image interfering factors, such as pixel-bleeding, light collection efficiency and pillow-shaped distortion (due to the galvo geometric distortion).
Other 2D systems based on real time detectors present good spatial resolution, suitable for applications in external radiotherapy, where spatial resolutions $\leq$ 2 mm are desirable [45, 46]. Such systems include the DOSIMAP, which is based on a plastic scintillator sheet and the strict discrimination of the scintillation with a camera, with a 2 x 2 mm spatial resolution [47, 48] or the BC-531 2D liquid scintillation system, using charge-coupled device camera, with spatial resolution of 1 mm^2 [49].

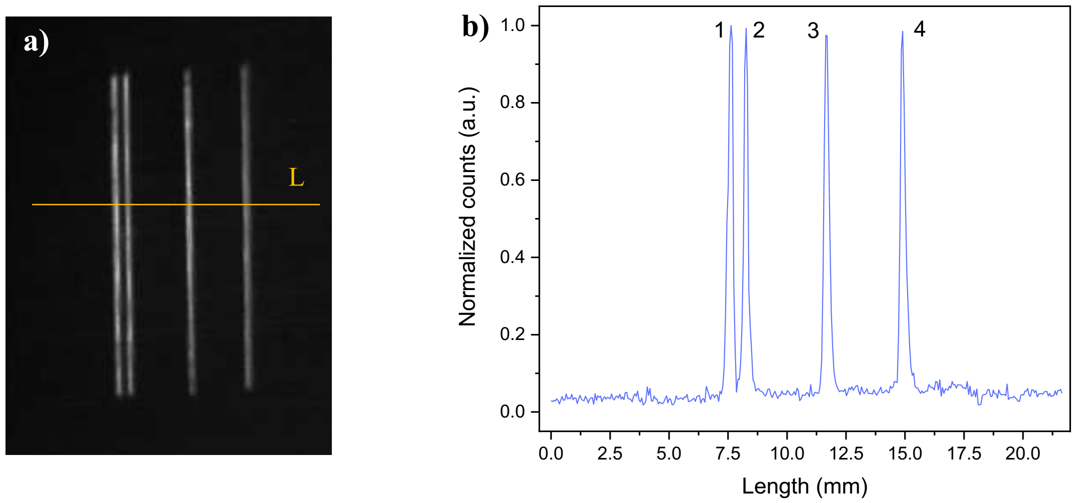

Figure 4. a) Teflon plate with four open slits on top of an A-CMg film irradiated with 6 MV photons, 600 MU/min and b) plot profile crossing line 'L', with slits identified

Table 4. Slit number, thickness, FWHM and difference between FHWM and slit thickness.

Slit nº	*Thickness (mm)*	*FWHM (mm)*	*Difference (%)*
1	1.0	1.1±0.1	10
2	1.0	1.1±0.1	10
3	1.5	1.6±0.1	7
4	1.5	1.6±0.1	7

3.4. Afterglow

Error! Reference source not found. Figure 5a presents the normalized RL counts versus time during and after irradiation for both A-C and A-CMg films, for a time span indicated in the plot. The beam is turned off at time $t = t_0 + 0.37$ seconds (vertical dashed line) and the signal from the Al_2O_3:C,Mg sheet (A-CMg) curve drops quickly to background, within 20 ms. One can observe, however, a delay to reach background for the Al_2O_3:C sheet (A-C). The counts decrease with time, reaching background 100 ms after the beam is off.
Figure 5 b shows the images from A-C acquired from t=0 ms ("beam off") until t=100 ms, in intervals of 20 ms. The brightness of the images decreases with time, which indicates an afterglow signal. Afterglow emission is due to radiative relaxation of unstable centres at room temperature and is a well-known effect in Al_2O_3:C dosimetric detectors, moreover 100 ms decay corresponds well to 35 ms Al_2O_3:C F-center lifetime [50]. Markey et al. [51] observed an afterglow for Al_2O_3:C lasting around 150 ms, 50 ms longer than what we measured with our films. In Markey's case, there was no separation between the emissions from different dosimetric centres, as is the case for our measurements, centred in the 420 nm emission (F-center). Two studies from Kalita et al. [52, 53] show comparable results as our A-CMg results, by not presenting any noticeable short-time fading or afterglow.

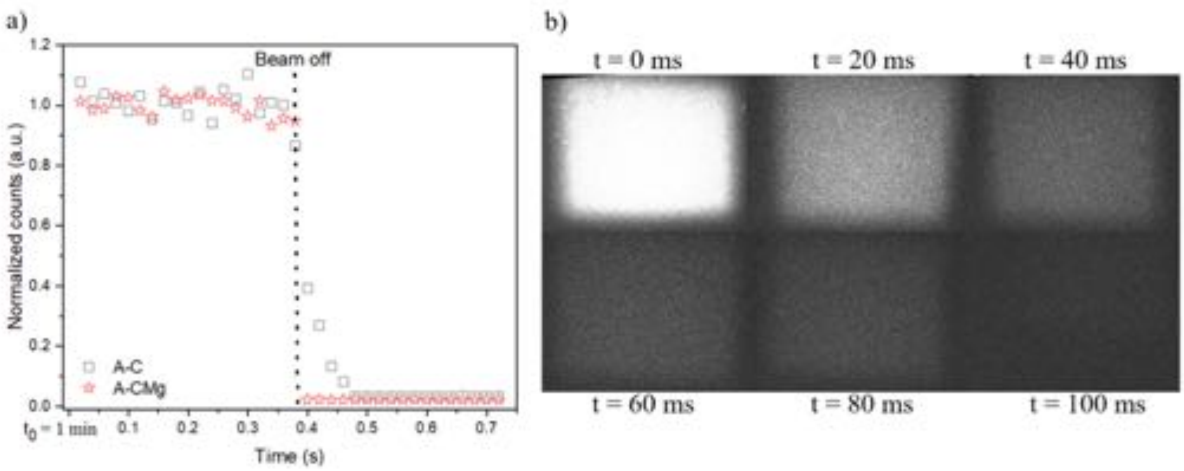

Figure 5. a) Normalized RL counts (to the maximum value) versus time for both A-C and A-CMg and b) images from the A-C films after the beam is turned off (dashed line) for six time spans (0, 20, 40, 60, 70 and 100 ms).

3.5. Dose rate

We measured the pixel intensities from A-C and A-CMg films for various given MU-rates provided at three different X-ray energies (6, 10 and 15 MV), in FF and FFF modes. All data are normalized to the 400 MU/min value.

Figure 6a shows the A-C averaged normalized pixel intensities from a 10 x 10 mm^2 ROI for different dose-rates, from irradiations with 6, 10 and 15 MV X-rays in FF mode. Dose rates ranged from 20 to 600 MU/min and a linear fit is plotted through the data points. The three curves are very similar, with slopes of 0.0025, 0.0025 and 0.0024 (MU^{-1}*min) for 6, 10 and 15 MV, respectively. The pixel intensities increase linearly with dose-rate ($R^2 \geq 0.999$). The standard deviation (1sd), not plotted in the graphs, are below 2% (for the dose rates ≥ 100 MU/min) and below 4% (for the dose rates < 100 MU/min). The upper plot demonstrates the residuals (%) between the measured pixel values and a perfect linear fit. A good overall agreement of ±1.5% is observed for dose-rates > 100 MU/min and of ±2.0% for dose-rates ≤ 100 MU/min.

Figure 6b plots the A-CMg averaged normalized counts from 10 x 10 mm^2 ROI for different dose-rates, from irradiations with 6, 10 and 15 MV X-rays in FF mode. Thanks to better CNR, the dose rates ranged from 5 to 600 MU/min. The signal of the images increased clearly linearly with the dose rate. The correlation coefficient of the linear fit was $R^2 = 0.999$ for 6 and 10 MV and 1 for 15 MV, with slopes of 0.0025 (15 MV) and 0.0024 (6 and 10 MV) (MU^{-1}*min). The standard deviations (1sd) are below 1% (for the dose rates ≥ 100 MU/min) and below 2% (for the dose rates < 100 MU/min). The upper plot presents the residuals (%) between measured pixel normalized values and a perfect linear fit. For the two lowest dose-rates (5 and 10 MU/min), the difference is around ±3.5% (due to lower pixel counting statistics), while the differences did not exceed ±1.5% for dose-rates ≥ 15 MU/min.

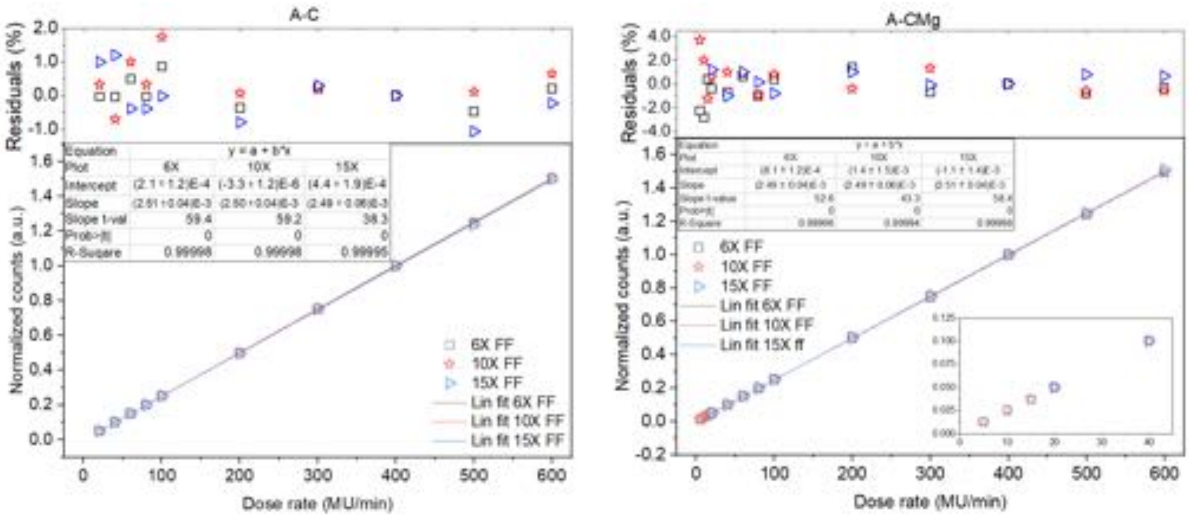

Figure 6. Dose rate dependence for 6, 10 and 15 MV irradiations, in FF mode, for a) A-C and b) A-CMg. Films are irradiated in 70 x 70 mm^2 field sizes, with 100 MU, ROI 10 x 10 mm^2, SSD = 100 cm. Linear regression (Lin fit), slope, slope t-value, Prob>|t| and R-square is presented in the plot. Standard deviations from the mean have an average < 2% (A-C) and < 1% (A-CMg) for dose rates above 100 MU/min, and < 4% (A-C) and 0.% (A-CMg) for dose rates below 100 MU/min.

The same measurements, with higher MU/min, were performed for films irradiated with 6 and 10 MV X-ray beams in FFF mode. Figure 7a shows the A-C average normalized signal versus dose rates for the two FFF beam energies. Although the fitted linear result has a $R^2 = 0.999$ (6 MV FFF), the curve does not intercept ‘0’, or a close value, as observed for the FF mode. The fitting for the 10 MV is $R^2 = 0.989$, with the curve not crossing ‘0’. The upper image presents the residuals (%) between the measured data and the reference from a perfect linear fit. The results from the 10 MV FFF difference curve indicates a supralinearity above 800 MU/min and a possible saturation starting around 2000 MU/min. Differences are, overall, worse than for the 6 and 10 MV in FF mode.

Figure 7b presents the plot from A-CMg film vs. dose rate for both 6 and 10 MV FFF. Better linearity is observed, when compared to the A-C film, with $R^2 = 0.999$ and an x-axis interception close to ‘0’ MU/min. The residuals observed in the upper plot indicates a deviation with reference below ±1.2%. No noticeable trend (supralinearity or saturation) is observed in any of the curves.

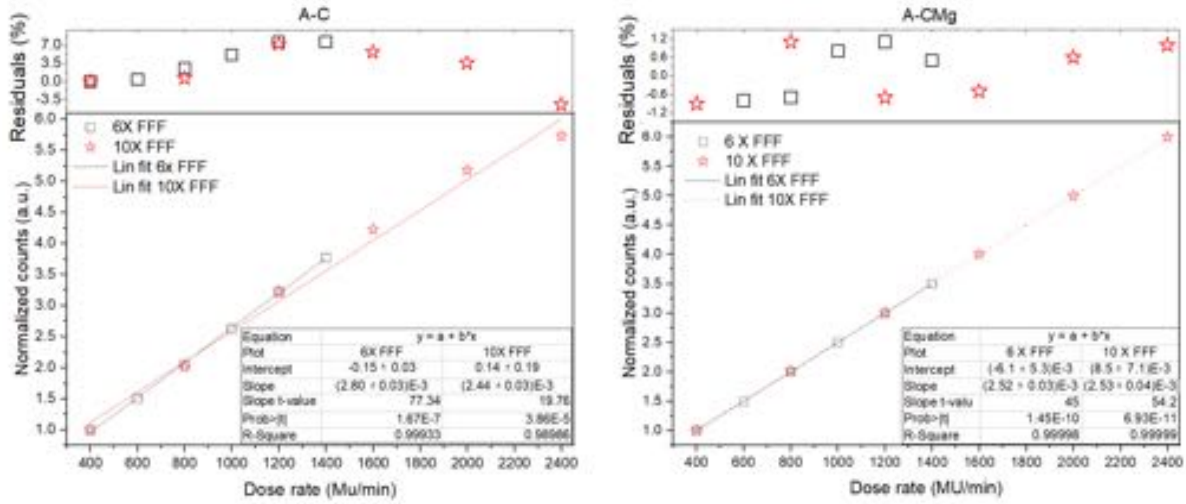

Figure 7. Dose rate dependence for 6 and 10 MV irradiations, in FFF mode, for a) A-C and b) A-CMg. Films are irradiated in 70 x 70 mm^2 field sizes, with 100 MU, ROI 10 mm^2, SSD = 100 cm. Linear regression (Lin fit), slope, slope t-value, Prob>|t| and R-square is presented in the plot. Standard deviations from the mean have an average of 1.5% (A-C) and 0.5% (A-CMg).

The slope from the A-CMg films in FF and FFF modes are very similar (0.0025), which indicates a consistent response with dose-rate. The same is not observed for the A-C films, with slopes of 0.0025 (FF) vs. 0.0028 (FFF) for 6 MV, and 0.0024 (FF) vs. 0.0025 (FFF) for 10 MV; while it is clear from Figure 7a that the fitted curve from 10X does not cross all the data points.

Previous results from RL point detectors showed good linearity with dose-rates, in both FF and FFF modes, when using optical fibre-based detectors with Al_2O_3:C crystals [3, 54]. Another study demonstrated that Al_2O_3:C and Al_2O_3:C,Mg 2D OSL films presented minimum detectable doses of 8 and 3 mGy respectively, for irradiations with 6 MV [55]. Al_2O_3:C,Mg RPL films, similar to L-CMg, published by Nascimento et al. presented linear dose response from 0.5 to 10 Gy, with supralinear behaviour observed between 10 and 70 Gy. For doses above 80 Gy, the detectors showed saturation. Another work, published by Akselrod et al. [56], using bulk single crystals of Al_2O_3:C,Mg observed a linear dose response from 0.5 to ≈200 Gy, where the signal saturates. The main difference between the results from Nascimento et al. and Akselrod et al. is the use of the F_2^+(2Mg) dosimetric centres (RPL), while in the results presented in Figures 6 and 7, the F-centres are measured (RL). When used as RPL detectors, Al_2O_3:C,Mg films present a residual fluorescence signal from non-irradiated 'as-grown' samples (F_2^+(2Mg)-centers), which explains the minimal detectable dose of 0.5 Gy, while when assessing the RL F centres, the minimal detectable dose is ≈ μGy.

We detected the individual pulses for the lowest dose rates from the LINAC and the A-CMg image from these pulses were translated directly to doses. In Table 5 we present the average ΔRL signals from pulses acquired under the lowest dose rates for 6, 10 and 15 MV (FF). The nominal dose per pulse from 15 MV is double the one from 6 and 10 MV and this can be also observed by the measured light intensity.

Table 5. Measured ΔRL for the given dose per pulse, for each nominal energy.

Nominal photon beam energy (MV)	Dose rate (Gy/min)	*ΔRL±sd*	*Dose per beam pulse (mGy/pulse)*
6	0.05	250±30	0.28
10	0.05	248±30	0.28
15	0.20	510±35	0.56

3.6 Small square fields and output factors

Shown in Figure 8 are examples of square fields measured with A-C films (upper row) and A-CMg (lower row), for fields of 100 x 100, 70 x 70, 50 x 50, 30 x 30 and 10 x 10 mm^2. The boundaries of the fields can be clearly seen for all the fields and film types. However, non-uniformities can be observed in the A-C images, due to the worse homogeneity of the films and the larger crystal size-. One can notice in the A-CMg films the shapes of the MLC, apparent from the form of vertical stripes from top to bottom.

The output factors from the films are presented in Figure 9a for 6 MV and Figure 9b for 10 MV. In both plots, the results reveal the RL signal fluctuations for A-C, especially for the smaller field sizes. These fluctuations correspond, on average, to ±5% standard deviation. The A-CMg profiles are clearly smoother than the A-C profiles, which results in better agreement with reference and smaller error bars (±2%).

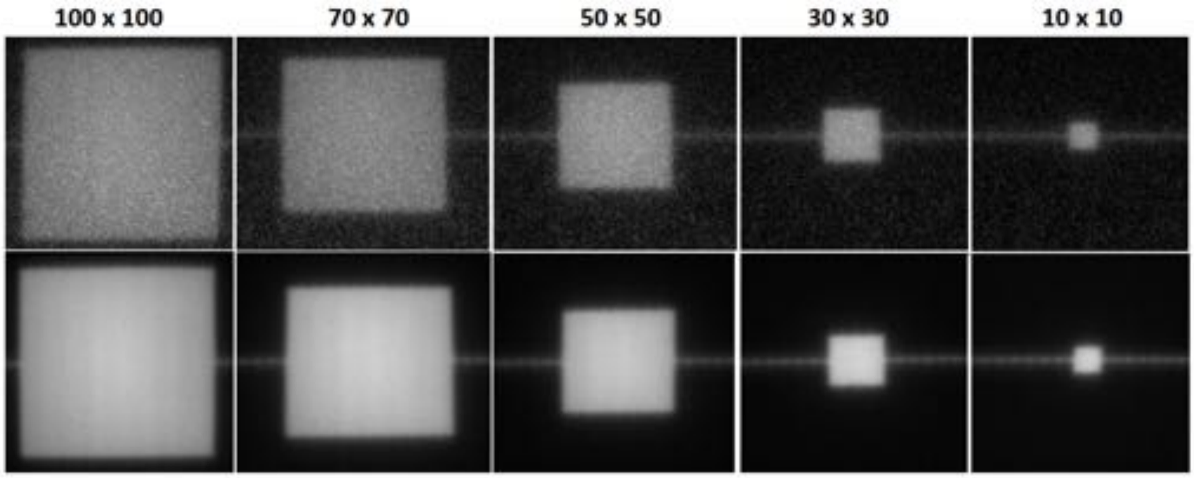

Figure 8. 2D square profiles from A-C films (upper sequence) and A-CMg films (lower sequence), for 100 x 100, 70 x 70, 50 x 50, 30 x 30 and 10 x 10 mm^2 in 6 MV FFF.

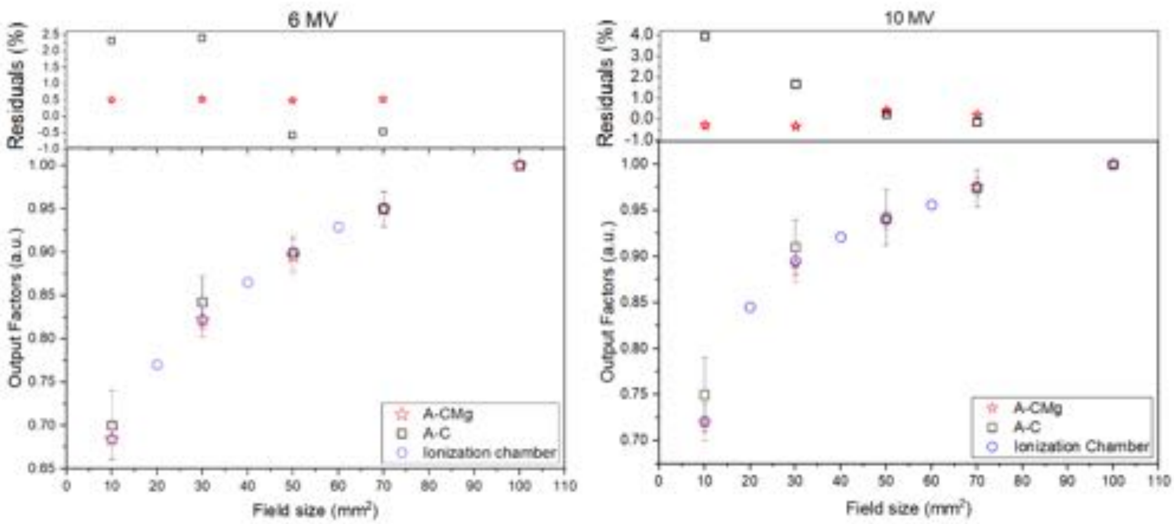

Figure 9. Plotted output factors normalized to 100 x 100 mm^2 from A-C and A-CMg films compared to reference (ionization chamber[57]) for a) 6 MV and b) 10 MV.

The largest differences were observed for the A-C output factors at 10 x 10 mm^2, with 2.4 % for 6 MV and 4% for 10 MV, whereas when looking at the A-CMg film the difference is lower, namely ±0.5%, for both energies. The A-CMg relative output factor presents a constant decrease with respect to the 100 x 100 mm^2. By comparison, the profiles of the same area of both films show that the apparent increase in dose closer to the edge of the fields can be mitigated by using the film with best homogeneity (Figure 4) and quality (CNR, Figure 3).
Our results are comparable to the 2D profiles obtained using Al_2O_3:C and Al_2O_3:C,Mg OSL films published by previous works [55, 58]. The OSL films, however, needed a correction algorithm to eliminate the effect of shallow traps and slow *F*-centre luminescence, in addition, the read out is passive, i.e., performed after the irradiation. Output factors measured using scintillators showed close agreement with reference using the ionization chamber for field sizes ≥ 20 x 20 mm^2. At smaller field sizes, the obtained output factors differed by 15% (6 x 6 mm^2) than those found using the ionization chamber [59].

3.7 Comparison between Al_2O_3:C and Al_2O_3:C,Mg films

The films based on Al_2O_3:C or Al_2O_3:C,Mg presented good results as a real time 2D detector using clinical beams. However, the films coated by AGFA with latest Al_2O_3:C,Mg powders have better uniformity and CNR, than the older films provided by Landauer. In addition, the AGFA-Al_2O_3:C,Mg film produces overall better results and gives the advantage of a wide dose rate range, with no afterglow.

At the end of the irradiation, a slight afterglow is visible for the A-C films, but the signal returns to the background level within approximately 100 ms. Overall, the impact of afterglow on practical use can be considered as small, since it causes an increase of the background contribution that must be subtracted from the total counts, only when repeated measurements are performed in a very short time. We did not observe any change in pixel intensity during continuous dose-rate irradiation (for several minutes), which could be caused by the interference of afterglow.

For A-C and A-CMg, the measured pixel intensities increase linearly with dose rate up to 600 MU/min (FF mode), and 2400 MU/min (FFF mode). The A-CMg film, however, is sensitive to the lowest dose rate delivered by the LINAC (5 MU/min) and has better overall agreement, with ±1.5% for FF mode, and ±1.2% for FFF mode. We were able to measure the single pulses for the lowest dose rates, for the three energies, showing the potential to measure integrated absorbed doses as low as 0.28 mGy. We did not observe any trend indicating overresponse or saturation.

Ultra-short pulsed high dose rate radiation therapy, known as FLASH, has recently created a serious ripple effect in the radiation oncology community. Pre-clinical data with electrons and protons has shown single-pulse doses above certain thresholds to decrease normal tissue radiotoxicity with a factor of nearly two, and as such increasing the differential response between healthy and tumor tissue [60, 61]. There's, now, no solid foundation for accurate dosimetry in supporting pre-clinical research to investigate the underlying radiobiological mechanisms of FLASH. Considering that preliminary data suggest that the dose per pulse seems to be a significant parameter, accurate dosimetry allowing dose assessment per pulse (dose-rate) will be mandatory. Our results do not indicate saturation to the highest dose rates in FFF mode (24 Gy/min) and we expect to validate our system at even higher dose-rate modalities, such as FLASH, where dose rates ranges from 40 Gy/s to 1000Gy/s.

When comparing squared small fields, again A-CMg presented better outcome than A-C. This is a result of better CNR, homogeneity and high spatial resolution. One of the challenges in QA is dosimetry in small field sizes, used, for example, during stereotactic body radiotherapy (SBRT) and Intensity modulated radiotherapy (IMRT), with various amounts of primary and secondary scattered photons, steep gradient of the radiation field, volume averaging effect, lack of charged particle equilibrium, partial occlusion of radiation source and beam alignment. The IAEA 483 (IAEA, Vienna, 2017) Code of Practice for small field dosimetry states that detectors suitable for small field dosimetry should have no, of low, energy dependence of the response, to measure with precision profiles and field output factors. Several centres relies on point detectors, as ion chamber and diode, which bring uncertainties in reproducibility and position. This can be overcome using 2D films and the good correlation between output factors from the A-CMg film and reference (ion chamber) shows potential for small field dosimetry. Further work will explore this application, by looking further into profiles and output factors in FF and FFF modes, in several photon energies.

Our system has a good spatial resolution, suitable for applications in external radiotherapy, where spatial resolutions ≤ 2 mm are desirable [62]. Good spatial resolution is an important parameter in QA for the dynamic MLC positional accuracy of the leaves and the accepted tolerance on the deviation between programmed and actual leaf position. Furthermore, there is a constant need for new systems for dosimetry in small animal irradiation, as this field provides an important tool used by preclinical studies to assess and optimize new treatment strategies such as stereotactic ablative radiotherapy. Characterization of radiation beams that are clinically and geometrically scaled for the small animal model is uniquely challenging for orthovoltage energies and minute field sizes [63].At such fields, we must improve the spatial resolution in one order of magnitude, to reach micrometre resolution, such as optical fibre based systems [64].

Ideally, every treatment session of every patient should be monitored with *in vivo* dosimetry so that the dose delivered is verified and recorded. Otherwise, there may be situations where a treatment error may go unnoticed. However, no automated dosimetry system is available and the labor and machine time required to perform *in vivo* dosimetry in every patient is unrealistic and not feasible in a busy radiotherapy clinic environment. We believe that our real time system can be explored for *in vivo* dosimetry by coating immobilization masks with Al_2O_3:C,Mg micro crystals. Virtually all head-and-neck patients nowadays are immobilized with masks that are individually made following the contours of each patient. This helps make the treatment as accurate and effective as possible. Conventional fractionation consists of daily treatments delivered for several days. The mask is worn during all the fractions to reposition the patient in an accurate manner. That makes it the perfect candidate for a patient specific QA dosimeter.

Although we focus on the development of an RL system for patient-specific QA, where RL films are placed on the skin of patients, or coated on immobilization devices, one could easily imagine application to dose-rate measurement during beam commissioning or annual QA checks. Once we demonstrated that good quality results can be acquired with single, or few images, acquisition of beam data could be performed in a fraction of the time needed when using conventional detectors, such as ionization chambers.

An observed possible limitation arises from stray radiation from the treatment head and photon interactions within the camera that strike the sensor, causing some single pixel saturation. The probability of such interactions increases with the number of delivered MU/min. A noise or median filter can remove these saturated pixels, but ideally, shorter acquisition times are ideal.

3.8. Conclusions

The measurements reported in this work present the potential of Al_2O_3:C and Al_2O_3:C,Mg RL films for clinical dosimetry in a wide range of tests including wide range of dose-rates and small fields sizes. We compared these films regarding their homogeneity, image quality, afterglow and spatial resolution.
The Al_2O_3:C,Mg type of film compare favorably with results obtained with reference detectors, such as ion chamber systems. In fact, the high sensitivity of Al_2O_3:C,Mg permits to measure real time dose-rate with high spatial resolution and good film homogeneity. This RL film is suitable for accurate determination of doses, as low as 0.28 mGy, as well as wide range of dose-rates, in FF and FFF modes. When output factors of different films are compared, A-CMg presents a good agreement with the reference data.
In conclusion, we have presented a system for accurate and safe delivery of radiation in clinical practice. This study differed from other real time systems in that the camera is placed at the head of the LINAC, facing the isocenter of the beam and the film. This simplified the need for corrections regarding the relative position of the camera, as it is always fixed in the same position related to the beam. Future work will focus on assessing the response of our real time RL system in specific clinical applications, for example, UHDR treatments (i.e. e-FLASH) and Volumetric modulated arc therapy (VMAT), as well as improving the spatial resolution for pre-clinical animal radiation and coat the radioluminescent material into immobilization devices.

Acknowledgement
The work presented in this article was partially supported by the Belgian Foundation against Cancer (Grant ID: FAF C/2016/842; link - https://www.kanker.be/project/team-van-professoren-luana-de-freitas-nascimento-dirk-verellen).

References

[1] A. Morono, E. Hodgson, Radioluminescence problems for diagnostic windows, Journal of nuclear materials, 224(1995) 216-21.

[2] L. Beaulieu, S. Beddar, Review of plastic and liquid scintillation dosimetry for photon, electron, and proton therapy, Physics in Medicine Biology, 61(2016) R305.

[3] LF. Nascimento, I. Veronese, G Loi, E Mones, F. Vanhavere, D. Verellen, Radioluminescence results from an Al2O3: C fiber prototype: 6 MV medical beam, Sensors Actuators A: Physical, 274(2018) 1-9.

[4] S. O'Keeffe, D. McCarthy, P. Woulfe, M. Grattan, A. Hounsell, D. Sporea, et al., A review of recent advances in optical fibre sensors for in vivo dosimetry during radiotherapy, The British journal of radiology, 88(2015) 20140702.

[5] A.S. Beddar, S. Law, N. Suchowerska, T.R. Mackie, Plastic scintillation dosimetry: optimization of light collection efficiency, Physics in Medicine & Biology, 48(2003) 1141.

[6] E. Mones, I. Veronese, A. Vedda, G. Loi, M. Fasoli, F. Moretti, et al., Ce-doped optical fibre as radioluminescent dosimeter in radiotherapy, Radiation measurements, 43(2008) 888-92.

[7] C.J. Marckmann, C.E. Andersen, M.C. Aznar, L. Bøtter-Jensen, Optical fibre dosemeter systems for clinical applications based on radioluminescence and optically stimulated luminescence from Al2O3: C, Radiation protection dosimetry, 120(2006) 28-32.

[8] P. Carrasco, N. Jornet, O. Jordi, M. Lizondo, A. Latorre-Musoll, T. Eudaldo, et al., Characterization of the Exradin W1 scintillator for use in radiotherapy, Medical physics, 42(2015) 297-304.

[9] P.E. Galavis, L. Hu, S. Holmes, I. Das, Characterization of the plastic scintillation detector Exradin W2 for small field dosimetry, Medical physics, 46(2019) 2468-76.

[10] J. Lambert, Y. Yin, D.R. McKenzie, S.H. Law, A. Ralston, N. Suchowerska, A prototype scintillation dosimeter customized for small and dynamic megavoltage radiation fields, Physics in Medicine & Biology, 55(2010) 1115.

[11] L. Archambault, A.S. Beddar, L. Gingras, R. Roy, L. Beaulieu, Measurement accuracy and Cerenkov removal for high performance, high spatial resolution scintillation dosimetry, Medical physics, 33(2006) 128-35.

[12] R. Zhang, D.J. Gladstone, L.A. Jarvis, R.R. Strawbridge, P.J. Hoopes, O.D. Friedman, et al., Real-time in vivo Cherenkoscopy imaging during external beam radiation therapy, Journal of biomedical optics, 18(2013) 110504.

[13] M. Guillot, L. Beaulieu, L. Archambault, S. Beddar, L. Gingras, A new water-equivalent 2D plastic

scintillation detectors array for the dosimetry of megavoltage energy photon beams in radiation therapy, Medical physics, 38(2011) 6763-74.
[14] P.Z. Liu, N. Suchowerska, P. Abolfathi, D.R. McKenzie, Real-time scintillation array dosimetry for radiotherapy: The advantages of photomultiplier detectors, Medical physics, 39(2012) 1688-95.
[15] W.J. Yoo, J. Moon, K.W. Jang, K.-T. Han, S.H. Shin, D. Jeon, et al., Integral T-shaped phantom-dosimeter system to measure transverse and longitudinal dose distributions simultaneously for stereotactic radiosurgery dosimetry, Sensors, 12(2012) 6404-14.
[16] I. Veronese, M. Cantone, N. Chiodini, A. Coray, M. Fasoli, A. Lomax, et al., Feasibility study for the use of cerium-doped silica fibres in proton therapy, Radiation measurements, 45(2010) 635-9.
[17] I. Veronese, N. Chiodini, S. Cialdi, E. d'Ippolito, M. Fasoli, S. Gallo, et al., Real-time dosimetry with Yb-doped silica optical fibres, Physics in Medicine & Biology, 62(2017) 4218.
[18] H. Zubair, A. Oresegun, A.M. Rahman, N.M. Ung, K.M. Sharif, M. Zulkifli, et al., Real-time radiation dosimetry using P-doped silica optical fiber, Measurement, 146(2019) 119-24.
[19] C.H. Jenkins, D.J. Naczynski, S.Y. Shu-Jung, L. Xing, Monitoring external beam radiotherapy using real-time beam visualization, Medical physics, 42(2015) 5-13.
[20] E.C. Ford, S. Terezakis, A. Souranis, K. Harris, H. Gay, S. Mutic, Quality control quantification (QCQ): a tool to measure the value of quality control checks in radiation oncology, International Journal of Radiation Oncology* Biology* Physics, 84(2012) e263-e9.
[21] M.S. Akselrod, A.E. Akselrod, S.S. Orlov, S. Sanyal, T.H. Underwood, Fluorescent aluminum oxide crystals for volumetric optical data storage and imaging applications, J Fluoresc, 13(2003) 503-11.
[22] M. Akselrod, V. Kortov, E. Gorelova, Preparation and properties of alpha-Al2O3: C, Radiation Protection Dosimetry, 47(1993) 159-64.
[23] E.G. Yukihara, S.W. McKeever, Optically stimulated luminescence: fundamentals and applications: John Wiley & Sons; 2011.
[24] M.S. Akselrod, A.E. Akselrod, New Al2O3: C, Mg crystals for radiophotoluminescent dosimetry and optical imaging, Radiat Prot Dosim, 119(2006) 218-21.
[25] S. McKeever, M. Akselrod, L. Colyott, N. Agersnap Larsen, J. Polf, V. Whitley, Characterisation of Al2O3 for use in thermally and optically stimulated luminescence dosimetry, Radiation Protection Dosimetry, 84(1999) 163-6.
[26] N.C.V. Stralingsdosimetrie, Code of practice for the absorbed dose determination in high energy photon and electron beams, Rep2008.
[27] N. Stuurman, N. Amdodaj, R. Vale, µManager: open source software for light microscope imaging, Microscopy Today, 15(2007) 42-3.
[28] M.D. Abràmoff, P.J. Magalhães, S.J. Ram, Image processing with ImageJ, Biophotonics international, 11(2004) 36-42.
[29] J. Schindelin, I. Arganda-Carreras, E. Frise, V. Kaynig, M. Longair, T. Pietzsch, et al., Fiji: an open-source platform for biological-image analysis, Nature methods, 9(2012) 676.
[30] F. Timischl, The contrast-to-noise ratio for image quality evaluation in scanning electron microscopy, Scanning, 37(2015) 54-62.
[31] Cell_Biology_group_of_Utrecht_University, How to quickly estimate SD of PSF in ImageJ, https://github.com/ekatrukha/DoM_Utrecht/wiki/How-to-quickly-estimate-SD-of-PSF-in-ImageJ, 2020.
[32] M.J. Norušis, SPSS 14.0 guide to data analysis: prentice hall Upper Saddle River, NJ; 2006.
[33] F. Lacroix, A.S. Beddar, M. Guillot, L. Beaulieu, L. Gingras, A design methodology using signal-to-noise ratio for plastic scintillation detectors design and performance optimization, Medical physics, 36(2009) 5214-20.
[34] B. Bechara, C.A. McMahan, W.S. Moore, M. Noujeim, H. Geha, F.B. Teixeira, Contrast-to-noise ratio difference in small field of view cone beam computed tomography machines, Journal of oral science, 54(2012) 227-32.
[35] F. Timischl, M. Date, S. Nemoto, A statistical model of signal–noise in scanning electron microscopy, Scanning, 34(2012) 137-44.
[36] G.V. Menon, R.S. Sloboda, Quality assurance measurements of a-Si EPID performance, Medical

Dosimetry, 29(2004) 11-7.
[37] J. Stützel, U. Oelfke, S. Nill, A quantitative image quality comparison of four different image guided radiotherapy devices, Radiotherapy and oncology, 86(2008) 20-4.
[38] J. Timmer, T. van Vuure, V. Bom, C. van Eijk, J. de Haas, J. Schippers, A scintillating GEM for 2D-dosimetry in radiation therapy, Nuclear Instruments and Methods in Physics Research Section A: Accelerators, Spectrometers, Detectors and Associated Equipment, 478(2002) 98-103.
[39] J. Tous, J. Blazek, J. Zemlicka, J. Jakubek, Evaluation of a YAG: Ce scintillation crystal based CCD X-ray imaging detector with the Medipix2 detector, Journal of Instrumentation, 6(2011) C11011.
[40] C. Andres, A. Del Castillo, R. Tortosa, D. Alonso, R. Barquero, A comprehensive study of the Gafchromic EBT2 radiochromic film. A comparison with EBT, Med Phys, 37(2010) 6271-8.
[41] S. Reinhardt, M. Hillbrand, J. Wilkens, W. Assmann, Comparison of Gafchromic EBT2 and EBT3 films for clinical photon and proton beams, Medical physics, 39(2012) 5257-62.
[42] L. Nascimento, W. Crijns, G. Goveia, Z. Mirotta, L. Souza, F. Vanhavere, et al., 2D reader for dose mapping in radiotherapy using radiophotoluminescent films, 129(2019) 106202.
[43] L.J. Meng, G. Fu, Investigation of the intrinsic spatial resolution of an intensified EMCCD scintillation camera, IEEE transactions on nuclear science, 55(2008) 2508-17.
[44] W. Crijns, D. Vandenbroucke, P. Leblans, T. Depuyd, A reusable OSL-film for 2D radiotherapy dosimetry, Physics in Medicine Biology, 62(2017) 8441.
[45] K. Otto, B.G. Clark, C. Huntzinger, Exploring the limits of spatial resolution in radiation dose delivery, Medical physics, 29(2002) 1823-31.
[46] N.C.V. Stralingsdosimetrie, N. Commissie, V. Stralingsdosimetrie, N.C.V. Stralingsdosimetrie, Code of practice for the quality assurance and control for intensity modulated radiotherapy, no June, (2013).
[47] V. Collomb-Patton, P. Boher, T. Leroux, J.M. Fontbonne, A. Vela, A. Batalla, The DOSIMAP, a high spatial resolution tissue equivalent 2D dosimeter for LINAC QA and IMRT verification, Medical physics, 36(2009) 317-28.
[48] L. Beaulieu, S. Beddar, Review of plastic and liquid scintillation dosimetry for photon, electron, and proton therapy, Phys Med Biol, 61(2016) R305.
[49] F. Pönisch, L. Archambault, T.M. Briere, N. Sahoo, R. Mohan, S. Beddar, et al., Liquid scintillator for 2D dosimetry for high-energy photon beams, Medical physics, 36(2009) 1478-85.
[50] L. Nascimento, F. Vanhavere, E. Silva, Y. De Deene, A short-time fading study of Al2O3: C, Radiation Physics and Chemistry, 106(2015) 26-32.
[51] B. Markey, L. Colyott, S. McKeever, Time-resolved optically stimulated luminescence from α-Al2O3: C, Radiation Measurements, 24(1995) 457-63.
[52] J.M. Kalita, M.L. Chithambo, A comparative study of the dosimetric features of α-Al2O3: C, Mg and α-Al2O3: C, Radiation protection dosimetry, 177(2017) 261-71.
[53] J.M. Kalita, M.L. Chithambo, The influence of dose on the kinetic parameters and dosimetric features of the main thermoluminescence glow peak in α-Al2O3: C, Mg, Nuclear Instruments and Methods in Physics Research Section B: Beam Interactions with Materials and Atoms, 394(2017) 12-9.
[54] C.E. Andersen, S.M.S. Damkjær, G. Kertzscher, S. Greilich, M. Aznar, Fiber-coupled radioluminescence dosimetry with saturated Al2O3: C crystals: Characterization in 6 and 18 MV photon beams, Radiation measurements, 46(2011) 1090-8.
[55] M.F. Ahmed, S. Eller, E. Schnell, S. Ahmad, M. Akselrod, O. Hanson, et al., Development of a 2D dosimetry system based on the optically stimulated luminescence of Al2O3, Radiation measurements, 71(2014) 187-92.
[56] M.S. Akselrod, A.E. Akselrod, New Al2O3: C, Mg crystals for radiophotoluminescent dosimetry and optical imaging, Radiation protection dosimetry, 119(2006) 218-21.
[57] Z. Feng, H. Yue, Y. Zhang, H. Wu, J. Cheng, X. Su, Monte Carlo simulation of beam characteristics from small fields based on TrueBeam flattening-filter-free mode, Radiation Oncology, 11(2016) 1-9.
[58] N. Shrestha, Further developments in 2D optically stimulated luminescence dosimetry based on Al2O3 and MgB4O7 2020.
[59] D.M. Klein, R.C. Tailor, L. Archambault, L. Wang, F. Therriault-Proulx, A.S. Beddar, Measuring output factors of small fields formed by collimator jaws and multileaf collimator using plastic

scintillation detectors, Medical physics, 37(2010) 5541-9.
[60] J. Hendry, Taking Care with FLASH Radiation Therapy, International Journal of Radiation Oncology, Biology, Physics, 107(2020) 239-42.
[61] R.M. De Kruijff, FLASH radiotherapy: ultra-high dose rates to spare healthy tissue, International journal of radiation biology, 96(2020) 419-23.
[62] A. Aalbers, M. Hoornaert, H. Palmans, Code of practice for the absorbed dose determination in high energy photon and electron beams, (2008).
[63] A. Vaniqui, B. van der Heyden, I.P. Almeida, L.E. Schyns, S.J. van Hoof, F. Verhaegen, On the determination of planning target margins due to motion for mice lung tumours using a four-dimensional MOBY phantom, The British journal of radiology, 92(2019) 20180445.
[64] T. Kurobori, Y. Yanagida, Y. Koguchi, T. Yamamoto, Variable periodic time operated fibre-coupled dosimetry system using Ag-activated RPL glasses with build-up, Radiation Measurements, (2020) 106300.

Luana de Freitas Nascimento – has a bachelor and M.Sc. in Physics from the University of Sao Paulo, Brazil, and also has received a double Ph.D. degree from Ghent University and Vrije Universiteit Brussel (Belgium) in 2015. Currently, she is a permanent researcher at the Research in Dosimetric Applications group from the Belgian Nuclear Research Centre, Belgium. Her research interests are focused on the medical dosimetry especially on luminescence dosimetry techniques.

Jo Goossens - Is a medical physicist at the Iridium Kankernetwerk Antwerpen with over 10 years of clinical experience. He has M.Sc in Chemistry and a M.Sc in Medical physics from KULeuven. His main interests are clinical implementation of new planning techniques and workflow management in a Radiotherapy department.

Paul Leblans - has a bachelor and M.Sc. in Chemistry from Antwerp University, Belgium, and received a Ph.D. degree from Antwerp University. He worked in R&D at Agfa since 1990 and developed phosphor materials and phosphor coatings for several applications. Currently, he is head of a group in the corporate innovation office of Agfa. His research interests are among others medical imaging and medical dosimetry.

Paul Sterckx - has a Bachelor degree for Industrial Chemistry from the Rega school in Leuven (Belgium) in 1986. He is doing product development for Agfa since 1988, since 2003 for Agfa Healthcare.

Filip Vanhavere – has degree of civil engineering and nuclear engineering from Ghent University, and received my PhD in applied physics also at Ghent University in 1999. Head of Expert Group Radiation Protection Dosimetry and Calibration at the Belgian Nuclear Research Centre SCK•CEN, and Vice-director of the Institute Environment, Health and Safety from SCK•CEN. Vice chair of EURADOS, Secretary of MELODI.

Lara Struelens – has a master in Physics from the Free University of Brussels and received a PhD degree in applied physics also at the Free University of Brussels in 2005. Since then she has been working as a researcher at the Belgian Nuclear Research Center on radiation dosimetry applications, with a main focus on medical applications. Since 2014, she is head of the SCK CEN research group on dosimetric applications. She is active member of EURADOS and member of the EURAMED scientific committee.

Mark Akselrod - is Chief Scientist and Executive Manager of Landauer, Inc. He manages Stillwater, Oklahoma, Crystal Growth Division of the company. His main research interests and achievements are in the field of radiation solid state physics, crystal growth, optical spectroscopy, luminescence dosimetry and optical data storage. He developed super sensitive Al_2O_3:C single crystals and Optically Stimulated Luminescent technique for radiation dosimetry commercialized by Landauer. Novel Al_2O_3:C,Mg crystals were developed and patented as two-photon absorbing volumetric Optical Data Storage (ODS) media and Fluorescent Nuclear Track Detector (FNTD). The results of research have been described in more than 100 papers published in peer reviewed scientific journals. He is also a co-author of 33 US patents.

Dirk Verellen – Is department head of Medical Physics Radiotherapy in the Iridium Kankernetwerk Antwerpen and is Professor of Biomedical Physics within the Faculty of Medicine and Health Sciences at Antwerp University (Belgium). He has a PhD in Medical Sciences from the Vrije Universiteit Brussel (VUB). His main field of interest is in the practical issues concerning implementation of high precision conformal radiotherapy and image-guidance in a clinical environment, also, establishing a safety culture in radiation oncology. He is amongst other services, member of the Board and the Physics Committee of the European Society for Radiotherapy and Oncology (ESTRO).